Journal of Alloys and Compounds, 197 (1993) 109–121
JALCOM 641

A covalent view of chemical bonding in Laves phases $CaLi_xAl_{2-x}$

Reinhard Nesper
Laboratorium für Anorganische Chemie, Eidgenössische Technische Hochschule, CH-8092 Zürich (Switzerland)

Gordon J. Miller*
Department of Chemistry, Iowa State University, Ames, IA 50011 (USA)

(Received December 16, 1992; in final form January 19, 1993)

Abstract

The series of compounds $CaLi_xAl_{2-x}$ was synthesized and structurally characterized in order to probe the effect of valence electron concentration on both global and local structural features in main group intermetallics. $CaLi_xAl_{2-x}$ compounds adopt Laves phase structures and show the following trend: (i) $x=0$, $MgCu_2$ type; (ii) $0.25<x<0.75$, $MgNi_2$ type; (iii) $0.80<x<1.0$, $MgZn_2$ type; (iv) $1.0<x<2.0$, two-phase region; (v) $x=2$, $MgZn_2$ type. Extended Hückel calculations are used to examine local chemical bonding effects and to rationalize the observed bond distance trends and arrangement of atomic constituents in this system.

1. Introduction

Binary compounds formed by the alkali or alkaline earth metals with elements from groups 13 or 14 provide systems on the borderline between typical metals and valence compounds. In particular, many phases with Li show not only features that resemble a b.c.c. packing of atoms, which is typical for many intermetallics, but also close contacts within the "anionic network", *i.e.* the arrangement of the group 13 or 14 atoms, which can be rationalized using the Zintl–Klemm–Busmann viewpoint. Is there a clear dichotomy in these two perspectives? Recent work on the Li–Si system shows that cation-centred energy levels can provide sufficient electronic stability and account for their dual characteristics [1].

Laves phases AB_2 form a family of intermetallic compounds whose structures have been explained as being dominated by the packing of spheres of different sizes [2, 3]. Laves himself stressed the importance of highest possible symmetry, highest degree of space filling and largest coordination numbers as determining factors for these structures**. At the same time he emphasized ambiguity of the use of atomic radii. In Mn_2Cu_3Al with the $MgCu_2$ structure, for example, the large aluminium atoms occupy the positions of the small copper atoms [4]. Some AB_2 compounds with the correct radius ratio of 1.225 do not form Laves phases, *e.g.* $ThAl_2$ which crystallizes in the AlB_2 structure type [5]. A model based on the packing of rigid spheres, which had been given by Laves and Parthé [6], was criticized by Pearson two decades ago [7].

More recently, Simon pointed out a general geometrical relationship between coordination numbers and structure types of Laves phases on the basis of a Vegard-like behaviour [8]. It seems, however, that the purely geometrical interpretation of structural relations between Laves phases and other AB_2 structures left more questions open than could be answered in a convenient way. Laves phases represent a class of intermetallic compounds that have received a tremendous volume of attention. With respect to space-filling arguments, these are typical intermetallics. They occur in three primary structure types, namely cubic $MgCu_2$, hexagonal $MgZn_2$ and $MgNi_2$ (see Fig. 1). A number of systematic studies of the various binary and some ternary variants indicate that the valence electron concentration (VEC) is a critical parameter determining their structures. Actually, the influence of an electronic factor on the formation of the structures of Laves phases was evident since their discovery, because the three classical structure types exist for different mean electron numbers per atom, *i.e.* for different VECs [9].

VECs in these systems have been discussed mainly as an overall VEC per atom (A and B) without drawing lines between the different chemical partial structures in these phases or considering an eventual electron transfer. Hafner presents an example of a change in

*Author to whom correspondence should be addressed.

**However, he stated that no other important factors should be present [4].

0925-8388/93/$6.00

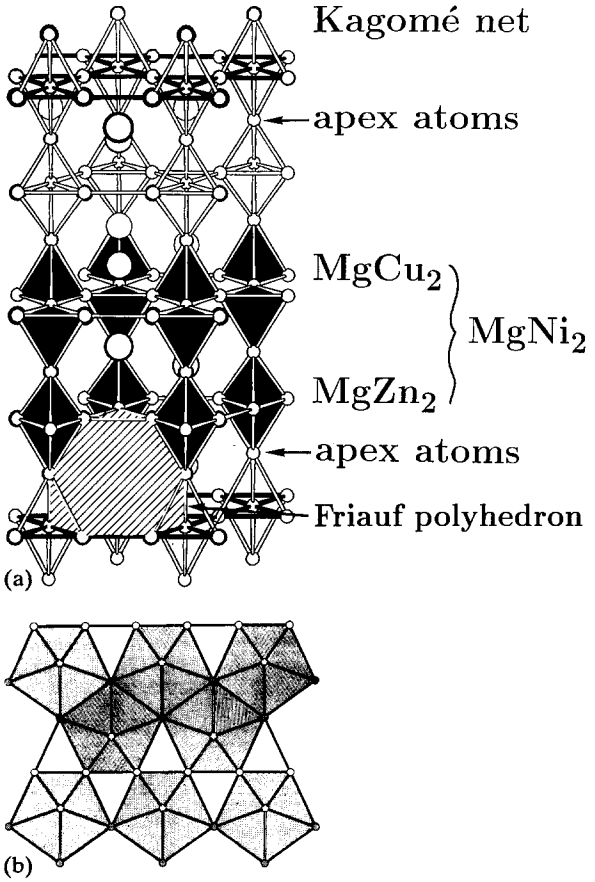

Fig. 1. (a) Features of the three primary Laves phases AB_2. Small open circles are B; large open circles are A. The top portion highlights the connectivity within the majority component B network, while the bottom portion emphasizes the polyhedra formed by the B atoms; tetrahedra in the $MgCu_2$-type and trigonal bipyramids in the $MgZn_2$ type. A atoms are surrounded by Friauf polyhedra of B atoms. (b) Projection of the Laves phase structure which highlights the description in terms of fused five rings.

the direction of electron transfer in the series $CaLi_2$, $CaMg_2$ and $CaAl_2$, where the majority component Li gives electron density to Ca, but Mg and Al gain increasingly negative charge [10]. According to his findings, one might argue that there is no preferred direction of electron transfer from one partial structure to another. However, inspection of the calculated electron density distributions clearly shows that the B frameworks, even in KNa_2, gain additional electron density, which peaks at the centres of the trigonal bipyramids formed by the sodium atoms. Such electron transfer is typical for semiconductors, namely the Zintl phases which follow traditional valence rules. The relationship among formal charge transfer from A to B atoms, VEC of the B atoms and B partial structures is known as the Zintl–Klemm concept [11]. This extremely successful, simple concept is based originally on two-centre two-electron bonds, but it can be expanded to multicentre interactions using preferred electron counts for polyhedral arrangements of atoms.

In this paper we describe our experimental and theoretical investigations of the ternary system Li/Ca/Al in order to probe local and global structural effects due to variations in VEC. No ternary compound has been known until now in this system. Experiments have been carried out on the pseudobinary cut $CaLi_2/CaAl_2$, in which variation in the Li:Al ratio allows changes in the VEC. $CaLi_2$ adopts the hexagonal $MgZn_2$ structure type and $CaAl_2$ occurs in the cubic $MgCu_2$ variant. Some other new ternary Li–Ca aluminides have been prepared and are presented elsewhere [12].

The experimental results are compared with electronic structure calculations using the extended Hückel (EH) *ansatz* [13] to examine and interpret structural characteristics in terms of chemical bonding effects.

2. Classical description of Laves phases

Pearson classified the Laves phases as a family of compounds which are polytypes of the $MgCu_2$ structure [7]. One of the basic building units of all polytypes is the Kagomé net (3636) which is formed by the B atoms (see Fig. 1). Layers of stacked Kagomé nets occur perpendicular to the [111] and [001] directions of the cubic $MgCu_2$-type and hexagonal $MgZn_2$-type structures respectively. The A atoms centre Friauf polyhedra and therefore have a coordination number (CN) 16 with 12 direct B neighbours arranged as a truncated tetrahedron. Four additional A atom neighbours form a large tetrahedron to complete the coordination polyhedron.

Another description of the $MgCu_2$ structure emphasizes layers of three fivefold rings which follow the Schläfli descriptor $35^3/3^35^2$ (Figure 1(b)) [7]. As the following section indicates, the intermixing of A and B atoms in the rings is not a helpful tool to understand the structures in terms of (local) chemical bonding.

A large number of stacking variants of 3636 nets is known, many of which have been detected by transmission electron microscopy [14–17]. Some of them are listed in Table 1 and displayed in Fig. 2. The simplest case occurs for the hexagonal $MgZn_2$ type, which has a two-layer AB sequence. A 50% mixture of cubic $\alpha\beta\gamma$ ($MgCu_2$-type) and hexagonal $\alpha\beta$ stacking results in the third classical structure type, the $MgNi_2$ structure. Besides these three rather simple arrangements, there are complicated polytypes with translational periods up to 90 Å. The latter ones especially give a strong indication that long-range forces are present in the structures of Laves phases. Such long-range interactions may be due to local covalent bonding effects, since they are widespread in the chemically related, semiconducting Zintl phases.

TABLE 1. Stacking variants of Laves phases in the pseudobinary systems $Mg(M,N)_2$ (M, N ≡ Ni, Cu, Zn, Ag) (after refs. 14–17)

No of layers	Stacking	Cubic–hexagonal sequence	Hexagonal fraction	Cubic/ hexagonal	Z	c (Å)	Type	Fig. 2
2	AB'	h_2	1.00	0	4	8.567	$MgZn_2$	I
8	AB'AB'A'CA'C	$(chhh)_2$	0.75	0.33	16	34.40	$MgAg_{0.06}Zn_{1.94}$	VI
14	AB'ABC'BC'B'AB	$(chhchhh)_2$	0.71	0.40	28	~60		
9	AB'ABC'BCA'C	$(chh)_3$	0.67	0.50	18	38.70	$MgAg_{0.13}Zn_{1.87}$	
6	ABC'B'AB'	chchhh	0.67	0.50	12	25.0	$MgCu_xAl_{2-x}$	IV
16	ABC'BCA'CAB'A' CA'C'BC'B	$(chhchhch)_2$	0.625	0.60	32	66.7	$MgCu_xAl_{2-x}$	
10	ABC'BCA'C'BC'B	$(chhch)_2$	0.60	0.67	20	43.00	$MgAg_{0.18}Zn_{1.82}$	VII
21		$(hhchhch)_3$	0.57	0.75	42	90.3	$MgAg_{0.2}Zn_{1.8}$	V
4	AB'A'C	$(ch)_2$	0.50	1.00	8	15.83	$MgNi_2$	III
3	ABC	c	0	∞	6	8.04	$MgCu_2$	II

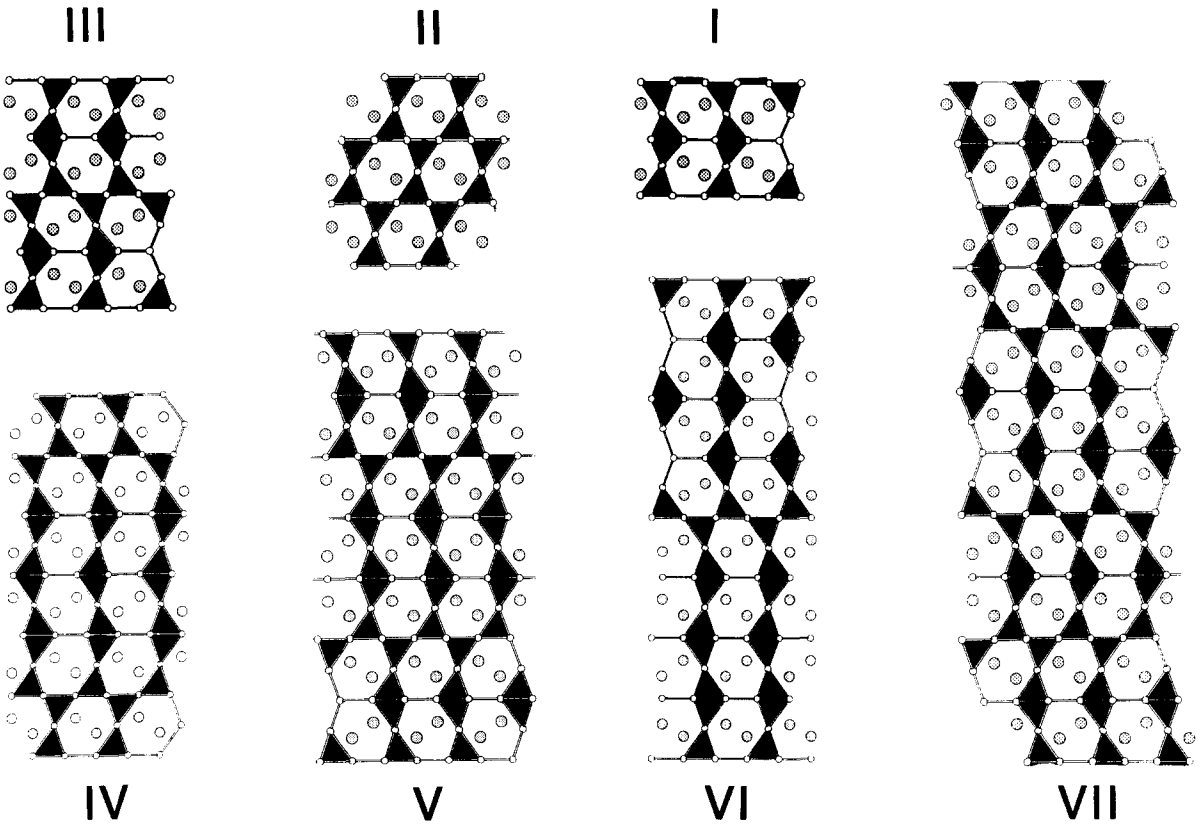

Fig. 2. Observed stacking variants of Kagomé nets which give numerous different Laves-type structures. Structure labels correspond to labels in Table 1.

3. Experimental details

In the three distinct binary systems Ca/Al, Ca/Li and Li/Al a variety of compounds with various structure types have been characterized (Ca/Al: $CaAl_2$, Ca_3Al_8, $CaAl_4$; Ca/Li: $CaLi_2$; Li/Al: LiAl, Li_3Al_2, Li_9Al_4). The highest melting point of these binary phases occurs for the relatively electron-rich $CaAl_2$ with $T_m = 1352$ K [18]. All other components and phases at the border of the ternary system melt below 1050 K. Therefore chemical syntheses were performed between 900 and 1200 K. The pure elements were weighed under an Ar atmosphere in an Mo crucible, which was then sealed in an Nb ampoule. The latter was protected against oxidation by an argon-filled quartz Schlenk tube. The Mo crucible is necessary because it withstands alloying with Al much more under the reaction conditions than Nb. Maximum temperatures were chosen as low as possible. Each sample was heated to melting temperature within 1–2 h, allowed to melt and finally cooled slowly in 1–3 days to room temperature.

All products exhibited a silvery, metallic lustre, but the Al-rich samples were relatively brittle while the

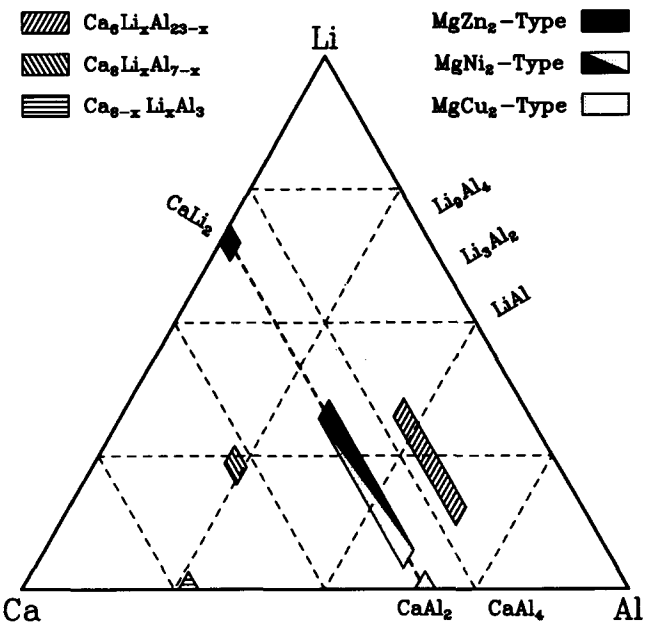

Fig. 3. The Ca/Li/Al ternary diagram identifying phases that have been structurally characterized, including this work [19].

Li-rich material showed pronounced ductility. A detailed X-ray structure determination for the different compositions provided the only fairly reliable analysis of these compounds, because a mechanical separation of heterogeneous products was unfeasible. Crystals of different compositions show practically no differences in appearance. Figure 3 gives some results of the investigations on the ternary system. There is no completely mixed crystalline variation from $CaLi_2$, with the $MgZn_2$ structure, to $CaAl_2$, with the cubic $MgCu_2$ arrangement. Between $CaLi_2$ and CaLiAl a two-phase region was detected, although both compounds have the hexagonal $MgZn_2$ structure. A continuous series of phases starts, however, at a composition near CaLiAl and ends at $CaAl_2$. In this series the structures change from $MgZn_2$ type through the $MgNi_2$ type to the $MgCu_2$ type with decreasing Li content.

4. Determination of crystal structures

Crystals suitable for X-ray diffraction measurements were selected from the product and checked for quality from Buerger precession photographs. Table 2 contains all crystal data and refinement parameters for the various samples in this study. Data for samples **4** and **8** were collected at room temperature with Mo Kα radiation (71.073 pm) on an Enraf-Nonius CAD4 diffractometer with variable scan speeds, a maximum scan angle of 2°, a graphite monochromator and $4.0° \leqslant 2\theta \leqslant 55°$. Lattice constants were determined via least-squares refinement on 25 reflections for $2\theta \leqslant 20°$. All structures were refined from appropriate structural prototypes [20, 21]. Tables

TABLE 2. Crystallographic data for Laves phases $CaLi_xAl_{2-x}$ (c/a refers to a two-layer $MgZn_2$ arrangement, $MgCu_2$ three layers, $MgNi_2$ four layers; V, volume per formula unit; N, measured, N', independent, $N'(3)$, independent reflections with $I \geqslant 3\sigma(I)$, N_p, parameters refined; R_{int}, internal consistency, R, unweighted, R_w, weighted R factor; o, pure type, m, mixed type or stacking faults; * calculated from cubic data). All phases except the cubic $CaAl_2$ belong to space group D_{6h}^4–$P6_3/mmc$ (No. 194)

No.	Composition	a (Å)	c (Å)	c/a	V(Å^3)	Z	N	N'	$N'(3)$	N_p	R_{int}	R	R_w	Type	Order
1	$CaLi_2$	6.268(2)	10.219(5)	1.630	86.92	4	540	147	113	11	0.038	0.055	0.037	$MgZn_2$	o
2	$CaLi_{0.93}Al_{1.07}$	5.838(2)	9.457(5)	1.620	69.76	4	431	116	92	13	0.041	0.081	0.044	$MgZn_2$	o
3	$CaLi_{0.89}Al_{1.11}$	5.816(2)	9.369(3)	1.610	68.62	4	2255	264	259	13	0.018	0.020	0.018	$MgZn_2$	o
4	$CaLi_{0.81}Al_{1.19}$	5.820(3)	9.366(5)	1.610	68.69	4	1073	132	125	13	0.022	0.025	0.025	$MgZn_2$	o
5	$CaLi_{0.70}Al_{1.30}$	5.796(3)	18.754(8)	1.618	68.20	8	763	214	153	29	0.050	0.041	0.033	$MgNi_2$	m
6	$CaLi_{0.70}Al_{1.30}$	5.795(1)	18.753(5)	1.618	68.17	8	444	201	159	29	0.023	0.033	0.035	$MgNi_2$	m
7	$CaLi_{0.33}Al_{1.67}$	5.734(1)	18.578(3)	1.620	66.13	8	1451	425	283	22	0.021	0.026	0.019	$MgNi_2$	o
8	$CaLi_{0.26}Al_{1.74}$	5.730(3)	18.564(9)	1.620	65.98	8	856	252	199	21	0.077	0.046	0.036	$MgNi_2$	m
9	$CaAl_2$	5.684*	13.922*	1.633*	64.92	6								$MgCu_2$	o

3 and 4 list the refined parameters for the various samples.

The molar volumes deviate considerably from Vegard-like behaviour. At $x \approx 1$ the greatest relative contraction occurs, showing that the ternary Laves phases around the composition CaLiAl are obviously predominantly stable as expected from simple thermodynamical arguments. No ternary phases have been detected for $x \leqslant 1$ and X-ray powder patterns show that samples of these compositions are heterogeneous. Compounds with $x \geqslant 1$ and $CaLi_2$ coexist in this field. The curve of Fig. 4 is fixed by the structure determinations of crystals **1–4** and **7** and by the data for $CaAl_2$ [4]. The compositions of samples **5**, **6** and **8** have been elucidated from the combination of site occupancies and volume data by using the curve in Fig. 4. Therefore in these cases the stoichiometric index x was adjusted according to the volume and then transformed into site occupation restrictions for the refinement of the corresponding data sets.

Furthermore, the c/a ratios show only a small variation, with the lowest value of 1.609 at $x = 1$. The change with x is not very significant. This fact, the large number of possible stacking variants found by Komura and coworkers [14–17] and the similarity of the bond distances justify the combined plot of volumes for cubic and hexagonal variants of the $MgCu_2$, $MgNi_2$ and $MgZn_2$ structure types. In this sense they may be understood as members of a quasi-continuous series. The $MgNi_2$ structure type then is the bridge between the purely cubic and purely hexagonal Laves phases, since it contains 50% cubically and 50% hexagonally surrounded layers.

Deviations from the given structure types occur as indicated in Table 4 by the symbol *. Crystal **8** exhibits very large temperature factors which are interpreted as an indication of stacking faults in the $MgNi_2$-type arrangement. We did not detect superstructure formation until now, although the expectation of superstructure formation is rather likely if one compares the results of Komura and coworkers for the ternary system $MgCu_xAl_{2-x}$ by electron microscopy.

Crystals **5** and **6**, like **8**, are at a borderline composition between simple structural arrangements, namely the purely hexagonal $MgZn_2$ type and the $MgNi_2$ type with the alternate stacking of cubically and hexagonally arranged Laves phase layers (see Fig. 2 for the three basic structure types). The Ca2 sites in crystals **5** and **6** show considerable deficiency, which gives rise to some difficulties in the interpretations. This is mainly due to the fact that either the missing electron density must be found at a position other than Ca21 and Ca22 or the composition has to deviate from $Ca_yLi_xAl_{2-x}$ with $y = 1$. The latter alternative is rather unlikely, because neighbouring phases with both larger (crystal **4**) and smaller (crystal **7**) volumes deviate from neither the AB_2 composition nor a Laves-type structure, though it cannot be rigorously excluded. It should be noted here that Kitano *et al.* have described structural misfits in Laves phases which really lead to a deviation from the AB_2 composition [22].

Twin models based on an intergrowth of [001] and [00$\bar{1}$] orientations have been checked extensively. They alone cannot really account for the lack of electron density on the Ca2 site and at the same time approach the composition expected from the unit cell volume.

There are two principal twinning possibilities: (i) $MgZn_2/MgNi_2$ and (ii) $MgNi_2/MgNi_2$ ([001]/[00$\bar{1}$])] intergrowth. Table 5 presents a correlation which shows those positions of the split model that belong to the two different orientations of the $MgZn_2$-type (A, B) and $MgNi_2$-type (C, D) structures respectively. From this table, those positions which are superimposed can be easily elucidated.

TABLE 3. $CaLi_xAl_{2-x}$-$MgZn_2$ types: atomic parameters, site occupations (SOF) and thermal parameters (pm^2). The coefficients of the anisotropic temperature factors are defined by $\exp[2\pi(h^2a^{*2} + \ldots + 2hka^*b^* + \ldots)]$

Atom	Site	Crystal	Parameter	SOF	U_{11}	U_{22}	U_{33}
Ca	4*f*	**1**	$z = 0.0627(2)$	100 Ca	341(8)	U_{11}	340(11)
		2	$z = 0.0599(3)$	100 Ca	193(13)	U_{11}	237(21)
		3	$z = 0.0600(1)$	100 Ca	170(2)	U_{11}	163(2)
		4	$z = 0.0606(1)$	100 Ca	211(5)	U_{11}	298(7)
M1	2*a*	**1**		100 Li	294(94)	U_{11}	337(130)
		2		72 Al, 28 Li	188(43)	U_{11}	219(50)
		3		75 Al, 25 Li	176(3)	U_{11}	163(4)
		4		73 Al, 27 Li	216(14)	U_{11}	374(17)
M2	6*h*	**1**	$x = 0.167(2)$	100 Li	257(48)	351(78)	331(63)
		2	$x = 0.164(1)$	47 Al, 53 Li	235(29)	217(38)	252(44)
		3	$x = 0.166(1)$	50 Al, 50 Li	179(3)	179(3)	153(4)
		4	$x = 0.167(3)$	55 Al, 45 Li	223(10)	226(12)	264(12)

TABLE 4. $CaLi_xAl_{2-x}$–$MgNi_2$ types: atomic parameters, site occupations (SOF) and thermal parameters (pm^2). The coefficients of the anisotropic temperature factors are defined by $\exp[2\pi(h^2a^{*2}+\ldots+2hka^*b^*+\ldots)]$. For the disordered phases (crystals **5** and **6**), two positions each have been refined for the sites Ca2, M1 and M3, for crystal **8**, all sites have been described by a contracted isotropic and an expanded anisotropic partial electron density. If U_{11} is marked by *, an independent refinement of both parameters was not possible and the isotropic temperature factor was fixed at a reasonable value. Relative Al and Li contributions are given for only the unsplit positions

Atom	Site	Crystal	Parameter	SOF	U_{11}	U_{22}	U_{33}	U_{12}
Ca1	4*e*	**5**	$z=0.0926(1)$	100 Ca	254(8)	U_{11}	47(8)	127(4)
		6	$z=0.0930(2)$	100 Ca	189(13)	U_{11}	73(14)	99(2)
		7	$z=0.0934(1)$	100 Ca	144(2)	U_{11}	149(3)	72(1)
		8	$z=0.0936(3)$	68 Ca	1957(49)	U_{11}	1482(44)	978(24)
			$z=0.0936(3)$	32 Ca	186(17)			
Ca21	4*f*	**5**	$z=0.8655(6)$	44 Ca	212(26)			
Ca22			$z=0.832(3)$	11 Ca	178(101)			
Ca21		**6**	$z=0.8696(1)$	46 Ca	161(42)			
Ca22			$z=0.840(5)$	7 Ca	352(140)			
Ca21		**7**	$z=0.8440(1)$	100 Ca	142(2)	U_{11}	152(3)	71(1)
Ca21		**8**	$z=0.8434(7)$	68 Ca	1988(49)	U_{11}	1453(44)	994(24)
Ca22			$z=0.8440(3)$	32 Ca	186(17)			
M11	4*f*	**5**	$z=0.140(1)$	63 Al	275(33)			
M12			$z=0.161(1)$	42 Al	239(42)			
M11		**6**	$z=0.133(3)$	24 Al	133(90)			
M12			$z=0.155(1)$	94 Al	350(34)			
M11		**7**	$z=0.1286(1)$	87 Al, 13 Li	158(4)	U_{11}	144(5)	79(2)
M11		**8**	$z=0.127(1)$	60 Al	1675(50)	U_{11}	1060(45)	837(25)
M12			$z=0.1286(7)$	21 Al	100*			
M2	6*g*	**5**		67 Al, 33 Li	206(9)			
		6		63 Al, 37 Li	171(17)			
		7		81 Al, 19 Li	160(5)	155(5)	169(4)	78(2)
		8		59 Al	1750(49)	1533(50)	1302(45)	766(25)
				20 Al	100*			
M31	6*h*	**5**	$x=0.166(5)$	33 Al	259(87)			
M32			$x=0.834(2)$	10 Al	221(33)			
M31		**6**	$x=0.168(8)$	47 Al	1087(171)			
M32			$x=0.835(2)$	17 Al	329(40)			
M31		**7**	$x=0.1638(2)$	83 Al, 17 Li	138(5)	152(5)	159(4)	70(4)
M31		**8**	$x=0.164(5)$	59 Al	1482(45)	U_{11}	1231(45)	785(41)
M32			$x=0.164(5)$	21 Al	100*			

On the basis of twin model (i), the intensities of the disordered phases **5** and **6** may be explained by a twinning of 20% $CaLi_{0.33}Al_{1.67}$ (**7**) and 80% $CaLi_{0.80}Al_{1.2}$ (**4**). Table 6 contains the normalized corrected intensities $|F|^2$ for the corresponding compositions. Clearly, there is no possibility of adding up the intensities of pure $MgZn_2$-type and pure $MgNi_2$-type stacking to those found for crystal **5** and crystal **6**, which are very similar. In this case the overlaid reflections $|F_{hkl}|^2$ with $l=2n$, which exist for both structure types, should have especially large values, while those with $l=2n+1$ should only scale the amounts of the different $MgNi_2$ contributions (C, D). The disordered crystals **5** and **6** really seem to have their own set of intensities which may be explained by an intergrowth of units that are smaller than the correlation length of the X-rays.

The refinement of only those reflections which arise from the $MgNi_2$ arrangement with $l=2n+1$ does not lead to a vanishing of the split positions of Ca, M1 and M3. This means that the $MgNi_2$ domains alone exhibit reorientations according to $[00\pm1]$ changes. By symmetry, Ca1 and M2 are not sensitive to these reflections, because they only contribute to those with even l indices.

An explanation of the observed data by twin model (ii) is not possible on the basis of the $MgNi_2$ arrangement. In the corresponding Laue symmetry 6/*mmm* the relation $|F_{hkl}|^2=|F_{hkl}|^2$ holds and therefore a $[00\pm1]$ twinning cannot lead to the large changes in the observed intensities as shown in Table 6.

The split positions observed for the Ca2, Al1 and Al3 sites are in agreement with both the twin model and a model which combines statistically distributed

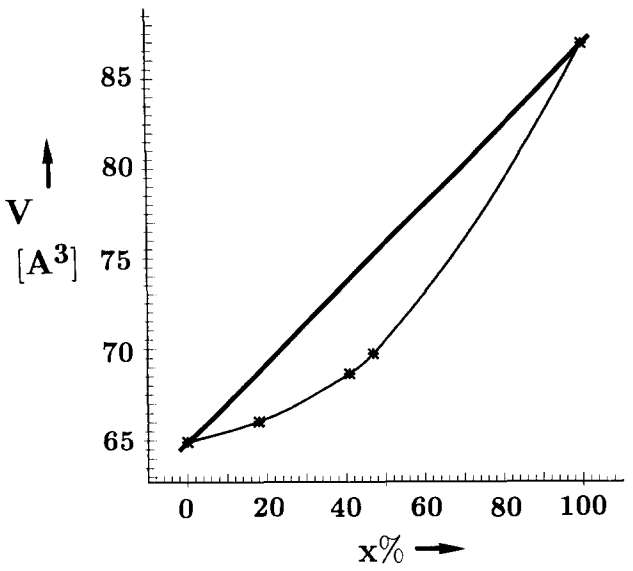

Fig. 4. Observed relationship between volume per formula unit and x in $CaLi_xAl_{2-x}$. The straight line corresponds to a Vegard-type (Zen-type) behaviour.

stacking sequences of the $MgCu_2$ and $MgZn_2$ types respectively in a ratio other than 1:1.

We clearly favour the description that there are changes in the stacking series of $MgZn_2$- and $MgCu_2$-type blocks including all orientations A–D for phases **5** and **6**.

One finds non-statistical residual electron density preferably near the split sites (Fig. 5), which can reduce the missing percentage of Ca to some extent. A second possibility is the existence of defects or partial replacement of lithium on the Ca2 sites. However, one is fairly unlikely to find 33% defects at one position in an intermetallic phase or that the small Li atoms could find a good coordination in the large voids of the Friauf polyhedron. On the other hand, one might think of a replacement of one Ca by two Li atoms, but this is unlikely as well, because there is no such effect in the Li-richer $MgZn_2$ type phases. Finally, we could imagine that $MgZn_2$ and $MgNi_2$ domains alternate and that at the domain boundaries a corresponding replacement occurs.

With further increasing Al content, we then observe variants of the $MgNi_2$-type structure with completely occupied Ca1 and Ca2 sites (crystals **7** and **8**) and without residual electron density at the split positions. Crystal **8** has the smallest volume of the ternary phases investigated so far. It represents the nearest approach to cubic $CaAl_2$. Inspection of Table 4 shows that the standard refinement in the $MgNi_2$ model yields in this case very large temperature factors for all atoms. Some attention was focused on the possibility of twinning or intergrowth with blocks of the cubic $CaAl_2$ structure. Interestingly, we found one and only one exception to the extinction rules of $P6_3/mmc$, the space group of the $MgNi_2$ type. Reflection 221 occurs with $F^2 \geqslant 25\sigma(F^2)$. The distance between corresponding planes in real space, $d(221, \text{hexagonal } MgNi_2) = 1.429$ Å, is very near to that of the rather strong reflection 440 in the cubic

TABLE 5. Correlation table of atomic positions for the $MgZn_2$-type (A, B) and $MgNi_2$-type (C, D) arrangements for the two orientations [001] (A, C) and [00$\bar{1}$] (B, D)

Position	Atom	$MgZn_2$	x	y	z	$MgNi_2$	Atom
a	Ca	A, B	0	0	0.09	C, D	Ca1
		A, B	0	0	0.41	C, D	
		A, B	0	0	0.59	C, D	
		A, B	0	0	0.91	C, D	
b	Ca	A	$\frac{1}{3}$	$\frac{2}{3}$	0.16	D	Ca21
		A	$\frac{1}{3}$	$\frac{2}{3}$	0.34	D	
		B	$\frac{2}{3}$	$\frac{1}{3}$	0.66	D	
		B	$\frac{2}{3}$	$\frac{1}{3}$	0.84	D	
c	Ca	B	$\frac{2}{3}$	$\frac{1}{3}$	0.17	C	Ca22
		B	$\frac{2}{3}$	$\frac{1}{3}$	0.33	C	
		A	$\frac{1}{3}$	$\frac{2}{3}$	0.67	C	
		A	$\frac{1}{3}$	$\frac{2}{3}$	0.83	C	
d	M1	A	$\frac{2}{3}$	$\frac{1}{3}$	0.13	D	M11
		A	$\frac{2}{3}$	$\frac{1}{3}$	0.36	D	
		B	$\frac{1}{3}$	$\frac{2}{3}$	0.63	D	
		B	$\frac{1}{3}$	$\frac{2}{3}$	0.87	D	
e	M1	B	$\frac{1}{3}$	$\frac{2}{3}$	0.13	C	M12
		B	$\frac{1}{3}$	$\frac{2}{3}$	0.36	C	
		A	$\frac{2}{3}$	$\frac{1}{3}$	0.64	C	
		A	$\frac{2}{3}$	$\frac{1}{3}$	0.386	C	
f	M2	A, B	$\frac{1}{2}$	0	0	C, D	M2
		A, B	$\frac{1}{2}$	0	$\frac{1}{2}$	C, D	
		A, B	0	$\frac{1}{2}$	0	C, D	
		A, B	$\frac{1}{2}$	$\frac{1}{2}$	$\frac{1}{2}$	C, D	
		A, B	$\frac{1}{2}$	$\frac{1}{2}$	0	C, D	
		A, B	0	$\frac{1}{2}$	$\frac{1}{2}$	C, D	
g	M2	B	$\frac{5}{6}$	$2x$	$\frac{1}{4}$	C	M31
		A	$\bar{x}$	$\overline{2x}$	$\frac{3}{4}$	C	
		B	$\overline{2x}$	$\bar{x}$	$\frac{1}{4}$	C	
		B	x	$\bar{x}$	$\frac{1}{4}$	C	
		A	$\bar{x}$	x	$\frac{3}{4}$	C	
		A	$2x$	x	$\frac{3}{4}$	C	
h	M2	A	$2x$	x	$\frac{1}{4}$	D	M32
		B	$\overline{2x}$	$\bar{x}$	$\frac{3}{4}$	D	
		A	$\bar{x}$	x	$\frac{1}{4}$	D	
		A	$\bar{x}$	$\overline{2x}$	$\frac{1}{4}$	D	
		B	x	$2x$	$\frac{3}{4}$	D	
		B	x	$\bar{x}$	$\frac{3}{4}$	D	

TABLE 6. Normalized corrected intensities $|F|^2$ for the $MgZn_2$, the mixed and the $MgNi_2$ structures represented by the compositions of crystals **4**, **5** and **7** respectively. Comparison of the reflections with the odd l index shows that there is a large difference between the mixed structures (**4** and **5**) and the pure $MgNi_2$ type (**7**)

d (pm)	hkl	**4** $MgZn_2$	**5**	**7** ($MgNi_2$)
0	000	10000	10000	10000
928.3	002		15	1
496.2	100	36	29	3
479.2	101		37	6
464.3	004	229	120	44
437.5	102	45	23	10
387.0	103		9	2
338.8	104	68	31	10
309.3	006		2	1
297.2	105		9	105
286.4	110	1740	1489	1282
273.8	112		1	0
262.6	106	1426	1139	1007
248.1	200	435	206	104
246.0	201		2	323
243.8	114	1931	1863	1788
239.6	202	1061	906	909
233.9	107		23	5
232.0	008	1047	1221	1320
230.3	203		14	207
218.8	204	64	22	31

structure, d(440, cubic $CaAl_2$) = 1.421 Å. Thus the measured intensity of the 221 reflection of the hexagonal data is likely just the contribution of blocks of cubic stacking. The dislocation of the two positions corresponds to a difference in the diffraction angle of $\Delta\theta = 0.1°$. Another possible cubic reflection which does not coincide with observed ones of the hexagonal setting is, by inspection of the d values, the 022 reflection.

5. Discussion

The phases $CaLi_xAl_{2-x}$ constitute an interesting series of Laves phases in which correlations between stoichiometry, electron count and structural features can be studied. The stoichiometry–volume relationship shows a clear deviation from a Vegard-like behaviour. There is, however, no completely mixed crystal behaviour in the range $0 \leqslant x \leqslant 2$. We find a two-phase field for $0 \leqslant x \leqslant 1$ and mixed crystals for $1 \leqslant x \leqslant 1.75$. The residual range $1.75 \leqslant x \leqslant 2$ needs further investigation. Both volume and phase stability behaviour may be understood by the development of the interatomic distances as given in Tables 7–9. There is a strong contraction of all interatomic distances between phase **1** and phase **2**, which seems to be due to the formation of Al–Al bonds. At the Li-rich side of the mixed crystal region

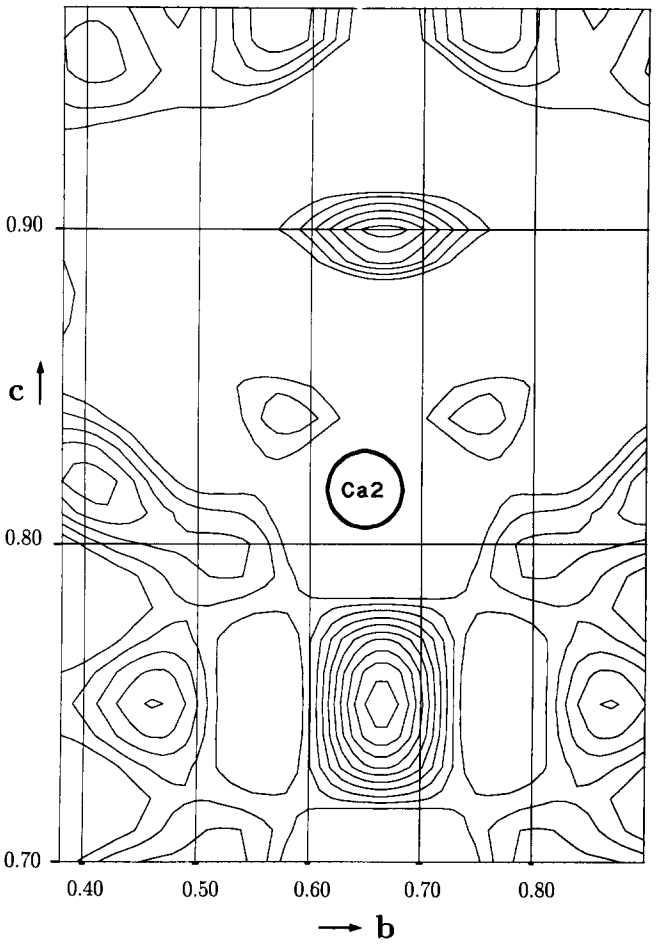

Fig. 5. Residual electron density surrounding the split Ca2 sites in crystals **5** and **6**.

TABLE 7. Interatomic distances (picometres) for the $MgZn_2$-type phases (n, multiplicity)

Atom pair	**1**	**2**	**3**	**4**	n
Ca–M2	367.2(12)	342.8(7)	335.4(2)	335.7(1)	6
M1	367.5(1)	339.3(5)	340.8(2)	340.5(1)	3
M2	367.5(9)	341.7(5)	340.8(2)	341.0(1)	3
Ca	382.7(4)	359.6(6)	354.7(2)	356.0(1)	1
Ca	383.9(2)	355.5(2)	354.6(7)	354.1(1)	3
M1–M2	312.7(10)	288.8(5)	288.5(1)	287.9(1)	6
Ca	367.5(4)	341.7(5)	340.8(2)	340.5(1)	6
M2–M2	312.4(30)	287.4(16)	288.5(1)	289.9(1)	2
M1	312.7(10)	288.8(5)	289.8(4)	287.9(1)	2
M2	314.4(30)	296.3(16)	292.2(4)	291.7(1)	2
Ca	367.2(12)	342.8(7)	340.8(2)	342.0(1)	4
Ca	367.6(9)	339.3(5)	335.4(2)	355.7(1)	9

(phase **2**) we find an occupation of about 75% Al on M1 and 50% Al on M2 (Table 3). Therefore the ternary phase becomes stable against $CaLi_2$ when three-quarters of all apical B atoms and every second atom in the Kagomé net are Al atoms. The residual contraction

TABLE 8. Interatomic distances (picometres) for phases **5–8** with the $MgNi_2$ metric lattice (n, multiplicity). For phases **5** and **6**, distances between split positions are not listed either if they are exclusively short or if they connect split positions M*mn* with the same index m. Distances of approximately reasonable magnitude, but between positions of different structure domains, are marked by *

Atom pair	5	6	7	8	n
Ca1–M2	337.8(2)	337.8(1)	335.1(1)	335.1(29)	6
M32	338.9(4)	338.6(3)	333.3(2)	332.9(25)	6
M31	338.9(4)	338.6(3)		332.9(25)	
M11	342.8(2)	342.3(1)	337.4(1)	337.1(3)	3
M12	343.1(8)	343.5(6)		337.1(3)	
Ca21–M2	332.4(7)	335.1(5)	338.8(48)	333.5(49)	3
M11	337.0(2)	337.5(1)	334.9(1)	335.2(3)	3
M31	342.0(6)	340.3(5)	335.7(2)	335.5(34)	6
M32	247.9(7)*	245.6(5)*		335.5(34)	3
Ca22	334.9(2)*	334.6(1)			3
Ca22–M2	343.5(17)	333.9(22)			3
M12	338.4(6)	336.7(4)			3
M32	335.4(11)	341.0(13)			6
M31	238.7(14)*	246.6(19)*			3
Ca21	334.9(2)*	334.6(1)*			3
M11–M31	278.2(7)	279.5(6)	281.5(2)	283.5(33)	3
M2	298.9(6)	297.4(5)	290.7(46)	299.0(48)	3
Ca21	337.0(2)	337.5(1)	334.9(1)	335.4(4)	3
Ca1	342.8(2)	342.3(1)	335.1(29)	336.6(4)	3
M12	334.6(2)*	334.6(1)*			3
M12–M32	276.8(28)	275.0(21)			3
M2	300.3(29)	302.2(22)			3
Ca22	338.4(6)	336.7(4)			3
Ca1	343.1(8)	343.5(6)			3
M11	334.6(2)*	334.6(1)*			3
M2–M2	289.8(1)	289.8(4)	286.7(1)	286.5(1)	4
M11	298.9(6)	297.4(5)	290.7(46)	288.0(48)	2
M12	300.3(29)	302.2(22)			
Ca21	332.4(7)	335.1(5)	334.9(1)	334.5(50)	2
Ca22	337.7(2)	333.9(22)			
Ca1	337.7(2)	337.8(9)	337.4(1)	335.1(29)	4
M321–M11	278.2(7)	279.5(6)	281.5(2)	283.5(31)	2
M31	287.5(11)	287.3(9)	281.8(2)	281.9(86)	2
M31	292.1(11)	292.2(9)	291.6(2)	291.1(86)	2
Ca1	338.9(4)	338.6(3)	333.3(2)	332.9(25)	2
Ca21	342.0(6)	340.3(5)	335.7(2)	334.9(36)	4
Ca22	238.7(14)*	246.6(19)*			2
M32–M12	276.8(28)	275.0(21)			2
M31	287.5(11)	287.3(9)			2
M32	292.1(11)	292.2(9)			2
Ca1	338.9(4)	338.6(3)			2
Ca22	335.4(11)	341.0(14)			4
Ca21	247.9(7)*	245.6(5)*			2

down to the binary $CaAl_2$ is only 22% of the complete contraction between $CaLi_2$ and $CaAl_2$.

In the ternary phases M1 is the apical position while M2 and M3 each form Kagomé nets. As mentioned before, the M2 net is never subject to disorder. Although the distances in the B partial structures in $CaLi_2$ and $CaAl_2$ are not differentiated among each other, there are considerable disparities in the ternary phases. The most significant contraction occurs between the apical site (M1) and the Kagomé nets, while the mean distances in the net reduce more slowly. The actual distances in the net split up into two different ones (see Table 8). As the relative Al content increases, so do the differences in these contact lengths. The same is true for the apical-to-net distances. They are discriminated rather clearly for the $MgNi_2$ variants with a maximum difference of about 20 pm (see M1–M2 and M1–M3 in Table 9).

TABLE 9. Development of interatomic distances from hexagonal $CaLi_2$ to cubic $CaAl_2$ for the ternary phases $CaLi_xAl_{2-x}$. The first row indicates the Al content in each phase

Atom pair	1	2	3	4	5	6	7	8	9
$(2-x)$	0	1.07	1.12	1.20	1.30	1.30	1.67	1.74	2.00
Ca1–M	367	342	338	338	339	339	335	335	333
Ca2–M	367	342	338	338	338	338	336	335	333
M1–M3	313	289	289	288	278	278	282	284	284
M2					300	300	291	288	284
M2–M2	312	287	289	290	290	290	288	287	284
	314	296	292	292					
M3–M3					288	288	282	282	284
					292	292	292	291	284

It seems that there is a tendency in these phases to favour alternating Kagomé nets with trigonal pyramidal nets. The distances M1–M3 here tend to be even slightly smaller than in the cubic $CaAl_2$ phase.

The distribution of distances and the site occupation for representative $MgZn_2$- and $MgNi_2$-type phases are shown in Fig. 6. These findings can be interpreted in terms of a clustering of Li-coordinated Al atoms in the ternary phases. These units can obviously crystallize preferably with a certain minimal Al content in the overall stoichiometry. In other words, Li coordination and Al cluster size seem to determine the Li:Al composition. The reduction in the Ca–M distances supports the idea of dominating Al–Al forces. Between phase **1** and phase **2**, d(Al–Al) shrinks 74% of the total reduction while the M–M bonds are at 78%.

6. Electronic structure calculations

Numerous investigations of the Laves phases in general have emphasized their structural characteristics via stacking of 3^6 and 3636 nets of atoms. We wish to exploit a different viewpoint based upon experience with other ternary intermetallic compounds involving

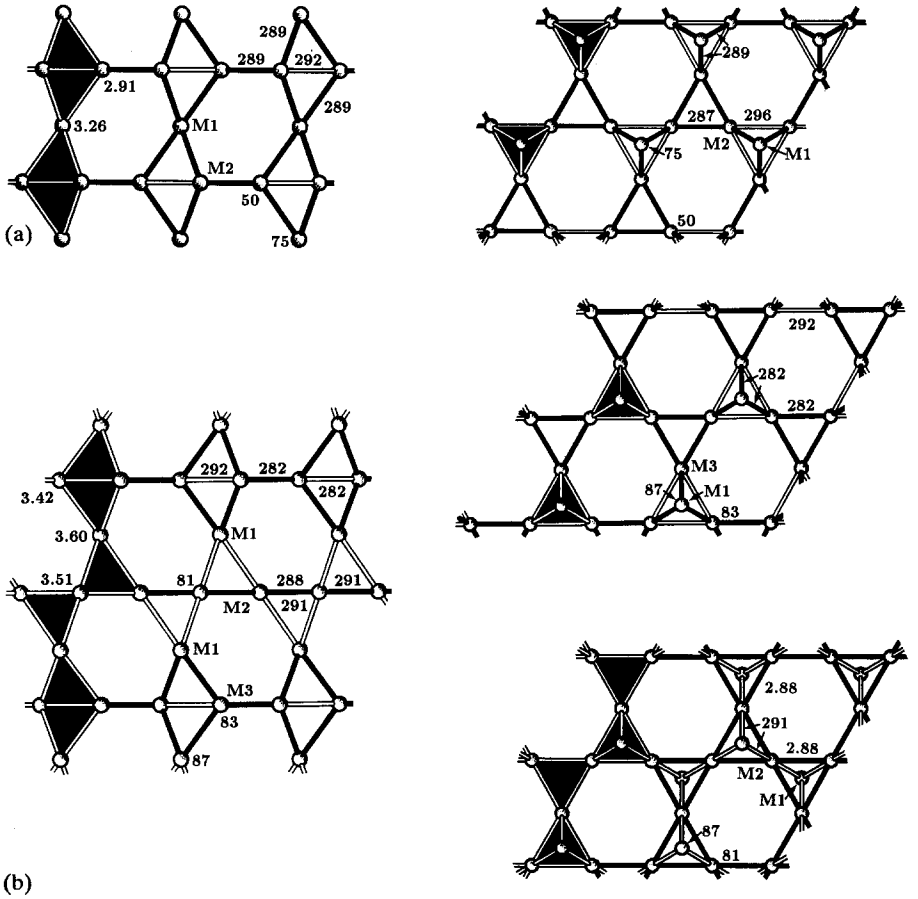

Fig. 6. Distribution of distances and site occupations in crystals **3** ((a) $MgZn_2$ type) and **7** ((b) $MgNi_2$ type). Bond distances are in picometres and site occupations are in percentages. (a) 2.91 and 3.26 are the calculated Mulliken populations for the sites indicated; (b) 3.42, 3.60 and 3.51 are analogous values. These values correlate with the fractional amount of Al at these positions.

Al as the electronegative species, namely a cluster approach.

Electronic band structure calculations have been performed on various models using the extended Hückel theory within the framework of the tight-binding approximation. Slater-type s- and p-functions were utilized for the atomic components (Ca: $\zeta(4s) = 1.10$, $H_{ii}(4s) = -7.0$ eV, $\zeta(4p) = 1.10$, $H_{ii}(4p) = -4.0$ eV; Al: $\zeta(3s) = 1.36$, $H_{ii}(3s) = -13.5$ eV, $\zeta(3p) = 1.35$, $H_{ii}(3p) = -6.5$ eV) and averages over the irreducible wedge in the appropriate Brillouin zones were obtained via special *k*-point sets.

We begin with the cubic structure of $CaAl_2$. The Al network is assembled from Al_4 tetrahedra, which are condensed to form an additional Al_4 tetrahedron, *i.e.* the primitive unit cell of the Al network in $CaAl_2$ contains two vertex-sharing Al_4 tetrahedra. The Ca atoms in the truncated tetrahedral holes form a diamond network. Let us first consider the Al network alone. Figure 7 illustrates the development of the total density of states (DOS) of this framework as isolated tetrahedra are brought together. At infinite separation, optimal chemical bonding occurs at 20 electrons per tetrahedron, as seen in P_4 (white phosphorus), As_4 and Sb_4. In terms of Wade's rules, we readily understand these structures as *nido*-trigonal bipyramids: six skeletal electron pairs, four-vertex deltahedra with four lone pairs. In molecular orbital terminology we can decompose the system into radial and tangential orbital components, which transform under the point group $4\bar{3}m(T_d)$ as $2a_1 + 2t_2$ (radial) and $e + t_1 + t_2$ (tangential). From Fig. 7(a) the lone pair orbitals are $a_1 + t_2$ centred around -7 eV and the bonding skeletal orbitals are $a_1 + e + t_2$ at -16, -11.3 and about -7 eV respectively. Only the t_1 skeletal antibonding level is shown; the corresponding antibonding t_2 orbital lies at about 5 eV. Of particular importance is the fact that this t_2 function at -7 eV is predominantly radially oriented.

Upon condensation, all orbitals broaden into bands and the lone pair t_2 levels are pushed up in energy. If we consider the condensation process, how does the formation of an additional tetrahedron per cell adjust the energy levels? For the outward-pointing radial orbitals (lone pairs), dispersion effects will be large; they represent, in effect, inward-pointing orbitals for the second tetrahedron. Thus we can identify why the

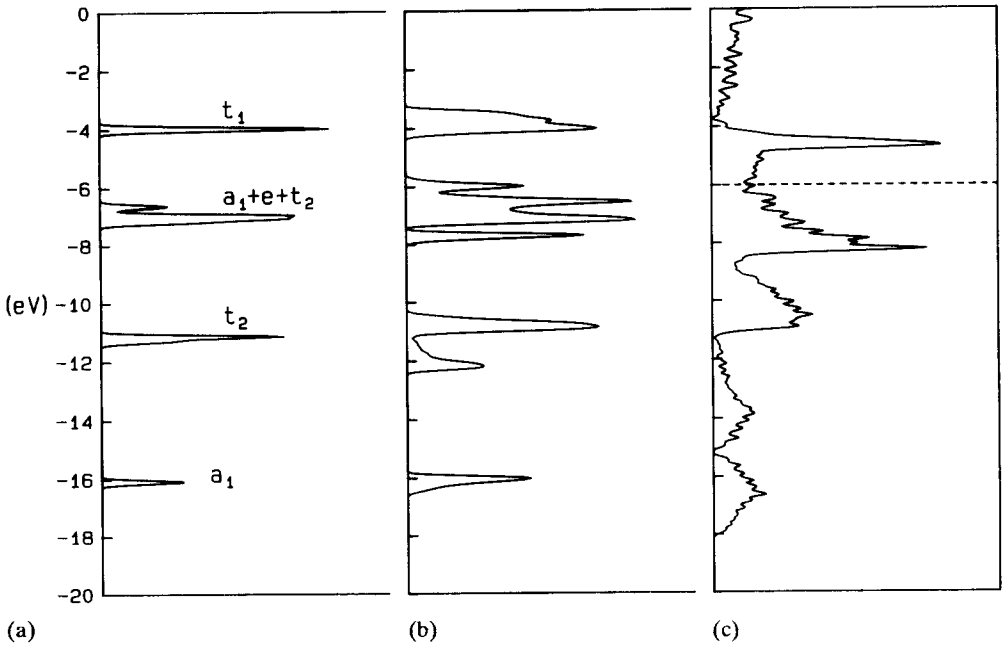

Fig. 7. Development of the total density of states (DOS) of cubic $CaAl_2$ as the Al_4 tetrahedra come closer together. (a) Separated by nearly 8 Å: orbitals are labelled according to the tetrahedral symmetry; (b) separated by 4.5 Å; (c) observed structure. The Fermi level for $CaAl_2$ is indicated by the dashed line.

t_2 orbitals are greatly destabilized. According to this line of reasoning, the optimal electronic stability should occur at 14 electrons per tetrahedron, *i.e.* Al_4^{2-}, which is confirmed by the crystal orbital overlap population (COOP) curve for the Al–Al interaction in this net (see Fig. 8). However, optimizing Al–Al bond strengths corresponds to $7/3 = 2.33$ electrons per atom in the cubic phase, but $CaAl_2$ has formally 2.67 electrons per atom. If we consider the Ca net, the diamond network is preferred for the half-filled band, cf. Si. Thus, in an s-only model, one electron per atom should maximize s-orbital interactions within the Ca net, *i.e.* Ca^+. Therefore, assuming no (weak) interactions between Ca and Al in $CaAl_2$, the one-electron theory projects $Ca^+(Al_2)^-$, which optimizes the chemical bonding situations in the two different networks. Although we should not explicitly neglect Ca–Al orbital interactions, as it turns out, they do not severely alter the previous picture. A large negative heat of formation ($\Delta H_F = -13.4$ kcal mol^{-1}) for $CaAl_2$ suggests strong internuclear bonding in this system. Hafner argues that the stability of $CaAl_2$ arises because the interatomic distances coincide exactly with the minima in the Al–Al and Ca–Ca pair potentials [10]. We can interpret his result as a renormalized size effect.

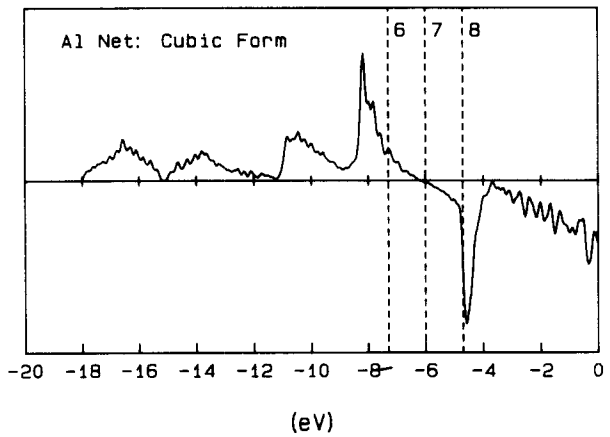

Fig. 8. Crystal orbital overlap population for the Al–Al interaction in cubic $CaAl_2$. The dashed lines correspond to the calculated Fermi levels for 6, 7 and 8 electrons per formula unit.

A similar tetrahedral cluster analysis for the hexagonal $MgZn_2$-type structure is complicated by the degree of symmetry lowering, which affects the valence orbitals. Certainly, as the energy difference curve in Fig. 9 attests, our simple methods account for experimental observations. Thus, since the trigonal bipyramid requires the same number of skeletal electrons as the tetrahedron, this five-atom cluster is stable for a lower electron/atom ratio than the four-atom cluster.

Electronic forces that influence the relative stabilities of these different structure types have been examined for systems involving transition metals [23]. Although local chemical bonding effects were not addressed in detail, the results clearly indicate that the different Laves phases – $MgCu_2$, $MgZn_2$ and $MgNi_2$ types – are favoured for specific regions of VEC.

Using second-moment-scaling techniques, Lee has extended our understanding of electronic factors controlling structures of AB_2-type intermetallic compounds

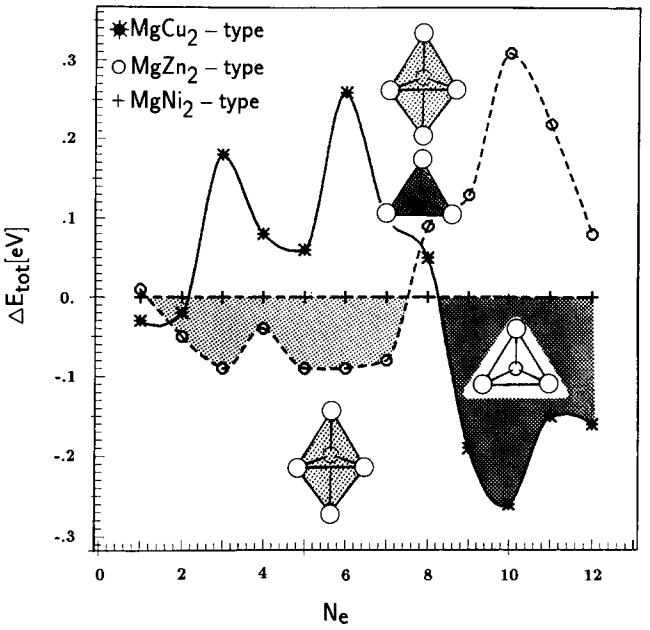

Fig. 9. Energy difference curves between $MgCu_2$-, $MgNi_2$- and $MgZn_2$-type structures (the $MgNi_2$ type was chosen as the reference). For VECs up to approximately 6.5 the $MgZn_2$ type is favoured (dotted region), between 6.5 and 8.2 the $MgNi_2$ type is favoured and greater than 8.2 the $MgCu_2$ type is preferred (crossed region).

[24]. In fact, when the method of moments is applied via a tight-binding model for systems with low VECs [25], structures with larger third moments (large number of three-membered rings) are preferred. Thus Laves' principles involving high symmetry, large coordination numbers and dense packing emerge owing to the significant number of three-membered rings in these phases. With an atomic s- and p-orbital basis, Fig. 9 indicates another third-moment effect between the $MgZn_2$ and $MgCu_2$-type structures. Since the trigonal bipyramid has a larger third moment per atom than the tetrahedron, we find another reason for our calculated energy difference curves via the topology (connectivity) of the valence orbital overlap. Thus local chemical bonding effects are important for establishing structural preferences in these systems, which have been considered as "typical intermetallics".

7. Atomic distributions and bond distances

In samples **4** and **8**, $CaLi_{0.88}Al_{1.12}$ and $CaLi_{0.33}Al_{1.67}$ respectively, we find two fundamentally different distributions of Li and Al atoms in the majority component network. To clarify this point, the symmetry of the cubic phase $CaAl_2$ demands only one sort of Al atom site. In the $MgNi_2$- and $MgZn_2$-type compounds, there are respectively three and two crystallographically inequivalent sites for the majority component. We observe in the $MgNi_2$-type material $CaLi_{0.33}Al_{1.67}$ a nearly uniform distribution of Li throughout the majority atom framework – each site is occupied by about 83% Al. On the other hand, the $MgZn_2$-type $CaLi_{0.88}Al_{1.12}$ begins to show differentiation in site preference – 50% in the Kagomé net and 75% in the apical positions.

Analysis of the corresponding Mulliken populations calculated for a homonuclear (Al) network at the appropriate electron counts for the two examples projects these two different distributions (Fig. 10). For the $MgZn_2$ case, at about 6.0 electrons per formula unit a significant charge separation occurs between the two inequivalent sites, with greater electron density building up on the apical sites. Larger Mulliken populations correspond to positions where the more electronegative atom would segregate. Thus we observe a non-uniform distribution of Li and Al in the $MgZn_2$-type structure, with Al site preference on the apical positions, though this occupation pattern is not exclusive.

For the $MgNi_2$ example the differences in Mulliken populations among the three sites are much smaller; this is confirmed by the more uniform arrangement of Li and Al in the net. Figure 10 illustrates these two effective charges as a function of electron count per formula unit for two structure types. At 6.5 electrons the largest charge difference occurs, which corresponds to the maximum electronic stability of the $MgZn_2$ type. As we move to more electron-rich (or electron-poor) systems, these differences become much smaller. At the count for $CaAl_2$ the maximum charge difference

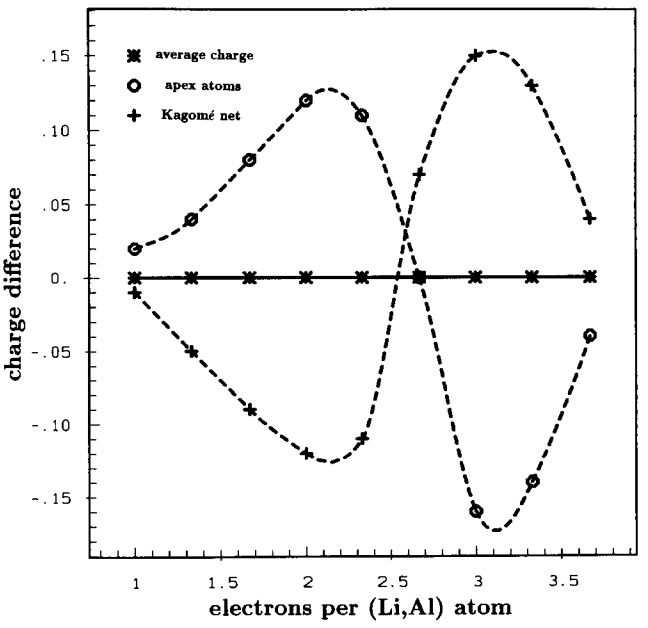

Fig. 10. Mulliken populations for atoms in the $MgZn_2$-type structure as a function of valence electrons per majority component. Open circles correspond to the apex atoms and crosses to the Kagomé nets (see Fig. 1).

is about 0.05 electrons. Therefore we find another compelling reason for the cubic phase at electron counts near 8 per formula unit – the tendency towards a uniform charge distribution in the majority component drives the structure to find an arrangement where, by symmetry, the electron density must be uniform.

In a recent article, Johnston and Hoffmann establish an orbital-based argument for the different bond distances, especially within the Kagomé nets, for intermetallics with the hexagonal $MgZn_2$-type structure [26]. Using both overlap populations and a fragment approach, they rationalize the contraction of the uncapped triangles relative to the other triangles capped by apical atoms. In the B network of $CaLi_xAl_{2-x}$ we find a similar trend in our computational results. At low values of x, for cases in which the distribution of Li and Al is nearly uniform, there is a significant distance disparity (see Table 9, M3–M3, Fig. 6). However, as x increases and there is an increasing site preference driving force to segregate Li and Al, this difference in bond distances becomes negligible. Limitations of the tight-binding approach that do not allow accurate inclusion of the random mixing of Li and Al in the Kagomé net restrict a proper population analysis as yet.

8. Summary

The ternary system $CaLi_xAl_{2-x}$ has allowed critical evaluation of the effect of valence electron concentration on structures in a system that is certainly intermetallic in nature yet sits near the metal–nonmetal border. In fact, we suggest that local chemical bonding effects, as seen by our adaptation of Wade's rules, are important. Also, given the preferred colouring pattern for Al atoms in compositions approaching CaLiAl, an intriguing hypothesis states that Zintl–Klemm concepts of localized bonding are important factors influencing the stoichiometric limit. Although structural determinations in $CaLi_xAl_{2-x}$ did not reveal unequivocal evidence for these ideas, we are pursuing further examples at the borderline between intermetallics and valence compounds in order to strengthen our understanding of chemical bonding in these solids.

References

1 M. C. Böhm, R. Ramírez, R. Nesper and H. G. von Schnering, *Ber. Bunsenges. Phys. Chem., 89* (1985) 465; R. Nesper and H. B. von Schnering, *J. Solid State Chem., 70* (1987) 48.

2 J. B. Friauf, *J. Am. Chem. Soc., 49* (1927) 3107.

3 F. Laves and H. Witte, *Metallwirtschaft, 14* (1935) 645; F. Laves, *Naturwissenschaften, 27* (1939) 65.

4 F. Laves, in J. Westbrook (ed.), *Intermetallic Compounds,* Wiley, New York, 1967, p. 129.

5 H. Klee and H. Witte, *Z. Phys. Chem., 202* (1954) 352.

6 E. Parthé, *Z. Kristallogr., 115* (1961) 52.

7 W. B. Pearson, *The Crystal Chemistry and Physics of Metals and Alloys,* Wiley, New York, 1972.

8 A. Simon, *Angew Chem., 95* (1983) 94; *Angew. Chem. Int.Edn. Engl., 22* (1983) 96.

9 W. Hume-Rothery, *J. Inst. Met., 35* (1926) 313.

10 J. Hafner, *From Hamiltonians to Phase Diagrams,* Springer, Heidelberg, 1987.

11 E. Zintl and G. Brauer, *Z. Phys. Chem. B, 20* (1933) 245; E. Zintl, *Angew. Chem., 52* (1939) 1; W. Klemm, *FIAT Review of German Science, Naturforschung und Medizin in Deutschland 1939–1946, Anorganische Chemie Teil IV,* DVB, Wiesbaden, 1949, Vol. 26, p. 103; W. Klemm and E. Hohmann, Alkalisilizide, Alkaligermanide, ihre Darstellung und einege wichtige Eigenschaften, *Internal Report,* Universität Münster, January 1947; H. Schäfer and B. Eisenmann, *Rev. Inorg. Chem., 3* (1981) 29; H.G. von Schnering, *Nova Acta Leopold., 59* (264) (1985) 165; in A. L. Rheingold (ed.), *Homoatomic Rings, Chains and Macromolecules of Main Group Elements,* Elsevier, Amsterdam, 1977, Chap. 14; *Rheinisch-Westfälische Akademie der Wissenschaften Vorträge,* No. 325, Westdeutscher, Opladen, 1984, p. 7; H. Schäfer, *Ann. Rev. Mater. Sci., 15* (1985) 1.

12 G. J. Miller and R. Nesper, *J. Alloys Comp., 185* (1992) 221

13 R. Hoffmann and W. N. Lipscomb, *J. Chem. Phys., 36* (1962) 2179, 3489; R. Hoffmann, *J. Chem. Phys., 39* (1963) 1397; J. H. Ammeter, H.-B. Bürgi, J. C. Thibeault and R. Hoffmann, *J. Am. Chem. Soc., 100* (1978) 3686.

14 Y. Komura, *Acta Crystallogr., 15* (1962) 770.

15 Y. Komura and Y. Kitano, *Acta Crystallogr. B, 33* (1977) 2496.

16 Y. Komura and K. Tokunaga, *Acta Crystallogr. B, 36* (1980) 1548.

17 Y. Komura and Y. Kitano, *Collected Abstracts XVth Cong. Int. Union of Crystallography, Bordeaux, 1990,* Abstract PS11.01.09.

18 T. B. Massalski, J. L. Murray, L. H. Bennett and H. Baker, *Binary Alloy Phase Systems,* American Society for Metals, Metals Park, OH, 1986.

19 R. Nesper and U. Häussermann, unpublished results, 1992.

20 G. M. Sheldrick SHELX76, *Programs for Crystal Structure Determination,* University of Cambridge, 1976.

21 G. M. Sheldrick, SHELXTL, *An Integrated System for Solving, Refining and Displaying Crystal Structures from Diffraction Data,* University of Göttingen, 1978.

22 Y. Kitano, Y. Komura, H. Kajiwara, *Acta Crystallogr. A, 36* (1980) 16.

23 R. Haydock and R. L. Johannes, *J. Phys. F: Met. Phys., 5* (1975) 2055; R. L. Johannes, R. Haydock and V. Heine, *Phys. Rev. Lett., 36* (1976) 372.

24 S. Lee, *J. Am. Chem. Soc., 113* (1991) 101.

25 J. K. Burdett and S. Lee, *J. Am. Chem. Soc., 107* (1985) 3050.

26 R. Johnston and R. Hoffmann, *Z. Anorg. Allg. Chem., 616* (1992) 105.